

Impact of nanoparticle size and lattice oxygen on water oxidation on NiFeO_xH_y

C. Roy^{1,5}, B. Sebok^{1,5}, S. B. Scott^{1,5}, E. M. Fiordaliso², J. E. Sørensen¹, A. Bodin¹, D. B. Trimarco¹, C. D. Damsgaard², P. C. K. Vesborg¹, O. Hansen^{1,3}, I. E. L. Stephens^{1,4}, J. Kibsgaard¹ and I. Chorkendorff^{1*}

NiFeO_xH_y are the most active catalysts for oxygen evolution in a base. For this reason, they are used widely in alkaline electrolyzers. Several open questions remain as to the reason for their exceptionally high catalytic activity. Here we use a model system of mass-selected NiFe nanoparticles and isotope labelling experiments to show that oxygen evolution in 1 M KOH does not proceed via lattice exchange. We complement our activity measurements with electrochemistry-mass spectrometry, taken under operando conditions, and transmission electron microscopy and low-energy ion-scattering spectroscopy, taken ex situ. Together with the trends in particle size, the isotope results indicate that oxygen evolution is limited to the near-surface region. Using the surface area of the particles, we determined that the turnover frequency was $6.2 \pm 1.6 \text{ s}^{-1}$ at an overpotential of 0.3 V, which is, to the best of our knowledge, the highest reported for oxygen evolution in alkaline solution.

Renewable energy technologies, such as wind turbines and solar panels, hold the potential to satisfy both rising global energy demand and mitigate CO_2 emissions^{1,2}. The intermittent nature of wind and solar energy means that energy storage is one of the most critical challenges as it limits their widespread implementation. One possibility is to store the energy in chemical bonds³. Thus far, one of the most promising means to convert electricity into fuels is water electrolysis, in which H_2 and O_2 gases are formed⁴. Their recombination to provide electrical energy only has water as a by-product, which makes it a clean process.

The hydrogen evolution reaction, which takes place on the cathode side during water electrolysis, is possible at minimal energy losses^{5,6}. However, the slow reaction kinetics of the anodic reaction, the oxygen evolution reaction (OER), involves the transfer of four electrons and four protons and so limits the efficiency of electrolyzers⁷. No electrode material approaches the equilibrium potential of 1.23 V on the reversible hydrogen electrode scale (V_{RHE})^{8–10}, which corresponds to the minimum energy needed for the reaction. Consequently, the widespread use of electrolyzers is contingent on improvements to the OER kinetics.

Although $\text{Ni}(\text{Fe})\text{O}_x\text{H}_y$ mixed electrodes were used even in the nineteenth century in alkaline electrolyzers¹¹, the science is still under intense debate^{12,13}. Pure NiO_xH_y is an inactive catalyst, but the activity drastically increases when Fe is intercalated into the structure^{12–16}, with the optimal activity for compositions between 10% and 50% Fe (ref. 13). There are two main hypotheses as to the role of Fe: (1) Ni is the active site and Fe affects its valency, which makes it more active^{17,18} or (2) Fe itself is the active site^{19–22}, as first evidenced by X-ray adsorption spectroscopy and density functional theory calculations¹⁹, and subsequently by electrochemical scanning microscopy²². Conversely, more recently, it was suggested that both Ni and Fe sites are directly involved²³.

Some studies indicated that the bulk, and not just the outer surface, of the catalyst is active. For example, Batchellor and Boettcher

reported a linear increase of the OER current as a function of catalyst loading up to ~ 450 monolayer equivalents²⁴. The notion of bulk activity was supported by a recent theoretical study²⁵ that found similar thermodynamics for the OER intermediates in the bulk of the material as for the (001) surface. However, Hu and co-workers showed that the apparent turnover frequency (TOF) of NiFeO_x decreases at high loading²⁶, which suggests either that thick samples are not as active or that the OER becomes readily transport limited.

Previous studies probed $\text{Ni}^{3+/4+}/\text{Ni}^{2+}$ redox chemistry on NiFeO_xH_y electrodes at $\sim 1.3\text{--}1.4 V_{\text{RHE}}$ using cyclic voltammetry (CV) and gravimetric analysis, and concluded that each nickel atom in the film contributes on average approximately one electron^{24,27}. This observation indicates that the entire film is electrochemically accessible, which motivates the hypothesis that oxygen evolution occurs between the nanosheets of the layered double hydroxide structure of the catalyst, and so blurs the distinction between surface and bulk¹⁴. Moreover, NiFeO_xH_y films, which are typically electrodeposited, are highly porous¹³. These various studies point to three possibilities: (1) the activity is confined to an outer surface, which may be large for porous materials, (2) the activity is confined to a near surface region in which there is ionic conductivity and electrolyte intercalated between the nanosheets and (3) bulk activity in which the entire material is active. This complicates the determination of the intrinsic activity, a critical step towards the design of more-efficient OER catalysts, and motivates the use of a model system with a known and well-defined surface area¹⁴.

Isotope labelling studies using ^{18}O and operando mass spectrometry are a powerful tool to distinguish surface from bulk catalysis²⁸. Most of the catalysts probed using this method have revealed at least some degree of lattice-oxygen involvement, including Au (ref. 29), IrO_2/Ti (ref. 30), Co_3O_4 spinel³¹, molecular cobaltate nanoclusters³², Ru-based catalysts^{28,33} and perovskite materials with a high metal–oxygen bond covalency³⁴. Others, which include Pt (ref. 35), oriented thin films of rutile RuO_2 (ref. 36) and perovskites with low

¹SurfCat, Department of Physics, Technical University of Denmark, Kgs. Lyngby, Denmark. ²Center for Electron Nanoscopy, Technical University of Denmark, Kgs. Lyngby, Denmark. ³Department of Micro- and Nanotechnology, Technical University of Denmark, Kgs. Lyngby, Denmark. ⁴Department of Materials, Imperial College London, Royal School of Mines, London, UK. ⁵These authors contributed equally: C. Roy, B. Sebok, S. B. Scott. *e-mail: ibchork@fysik.dtu.dk

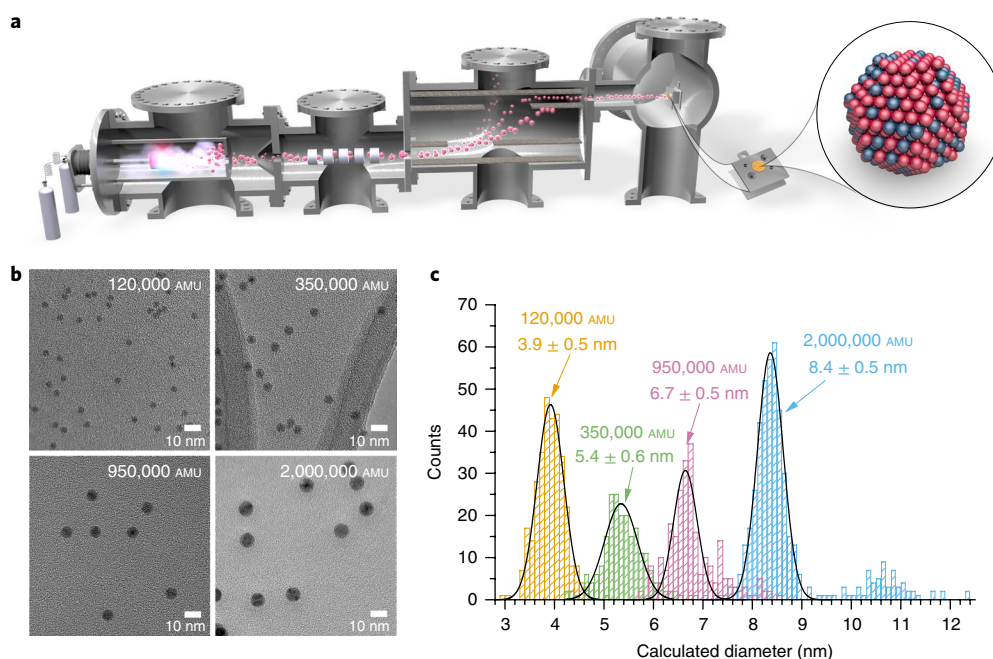


Fig. 1 | Deposition of mass-selected nanoparticles. **a**, A d.c. magnetron sputtering, gas-aggregation mass-selected nanoparticle source with lateral time-of-flight mass filter. Mass selected NiFe nanoparticles were deposited on polycrystalline gold disks for the activity measurements. **b**, TEM images of four different masses of NiFe nanoparticles. **c**, Size distributions, determined using the diameter measured on the TEM images in **b**, show the average size and 2σ for each mass deposited.

metal–oxygen bond covalency³⁴, have not. Shao-Horn and co-workers observed that lattice exchange occurs with materials that have a catalytic activity that is pH dependent, which indicates decoupled proton and electron transfers in the OER mechanism³⁴. Based on that argument, Ni(Fe)O_xH_y, which shows a higher catalytic activity in a stronger alkaline electrolyte, should also show participation of lattice oxygen³⁷. However, to the best of our knowledge, no studies have probed Ni(Fe)O_xH_y using isotopically labelled water, even though it is the catalyst of choice for industrial water electrolysis.

Such isotope studies consist of preparing the NiFeO_xH_y catalyst with one oxygen isotope (¹⁶O or ¹⁸O) or isotopic ratio, and then monitoring the O₂ products during oxygen evolution in an electrolyte that has a different isotopic ratio using a mass spectrometer (¹⁶O₂ at $m/z=32$, ¹⁶O¹⁸O at $m/z=34$ and/or ¹⁸O₂ at $m/z=36$). Should the O₂ that is evolved differ in isotopic composition from the electrolyte, then it is probably derived from the lattice oxygen or from water molecules intercalated between the layered nanosheets.

To draw a conclusion on the participation of lattice oxygen requires high sensitivity and thorough characterization: (1) to ensure that the isotopic oxygen is included in the NiFeO_xH_y catalyst, (2) to correctly identify whether it is evolved during the OER and, if so, (3) to quantify accurately the amount. To satisfy these requirements, we used a microchip-based electrochemistry–mass spectrometry (EC–MS) technology that has a high sensitivity. For example, it can detect 0.05 monolayer equivalents of H₂ desorbing from a flat Pt surface with a signal-to-noise ratio of ~20 (ref. ³⁸). We complement the operando mass spectrometry experiments with postcharacterization by low-energy ion scattering (LEIS) spectroscopy, a surface sensitive technique that enables the differentiation of ¹⁶O and ¹⁸O.

In this study, we prepared size-selected NiFe particles using a magnetron sputtering nanoparticle source (Fig. 1a). This physical synthesis method yields homogeneous, monodisperse and chemically pure metallic particles, with a well-defined size and loading, ideal for fundamental studies^{39,40}. We compared the nanoparticles to NiFeO_xH_y electrodeposited thin films. We tested the catalytic activity

using a rotating disk electrode assembly in 1.0M KOH, in which the particles oxidize under operando conditions. We complemented these experiments with X-ray photoelectron spectroscopy (XPS), high-resolution transmission electron microscopy (HRTEM) and scanning electron microscopy (SEM), and performed isotope studies as described above. The nanoparticle samples function as a model system with a well-defined and tunable surface area.

Together, the nanoparticle model system, extensive characterization and isotope studies enabled us to answer two fundamental questions: (1) What is the intrinsic activity of the active sites on a well-defined surface of NiFeO_xH_y; (2) Does lattice oxygen participate in the reaction?

Results

NiFe model system. Figure 1b shows TEM images of the as-prepared nanoparticles. Figure 1c shows the size distribution of the as-prepared nanoparticles. The size distribution was determined from the TEM images as described in Supplementary Note 1. As presented in Fig. 1b, all the nanoparticles have a regular and spherical shape regardless of their mass. The average particle diameters were 3.9 ± 0.5 nm, 5.4 ± 0.5 nm, 6.7 ± 0.6 nm and 8.4 ± 0.5 nm, respectively, for the four selected masses (Fig. 1b,c). There was a small population of larger particles with double the intended mass, which resulted from doubly charged nanoparticles, especially in the case of the 8.4 nm particles.

Stability and effects of OER operating conditions. The 6.7 nm nanoparticles were characterized with LEIS and XPS, as shown in Fig. 2a,b, respectively. The LEIS spectra of the as-deposited nanoparticles (green curve) showed clear Ni and Fe peaks, which cannot be differentiated due to the small difference between their atomic masses. After electrochemical testing (blue curve), the LEIS spectra showed additional features identified as K, O and C, most probably from residual KOH electrolyte, nanoparticle oxidation and air exposure. XPS spectra (Fig. 2b) of the as-deposited nanoparticles revealed metallic Ni and Fe. XPS analysis after

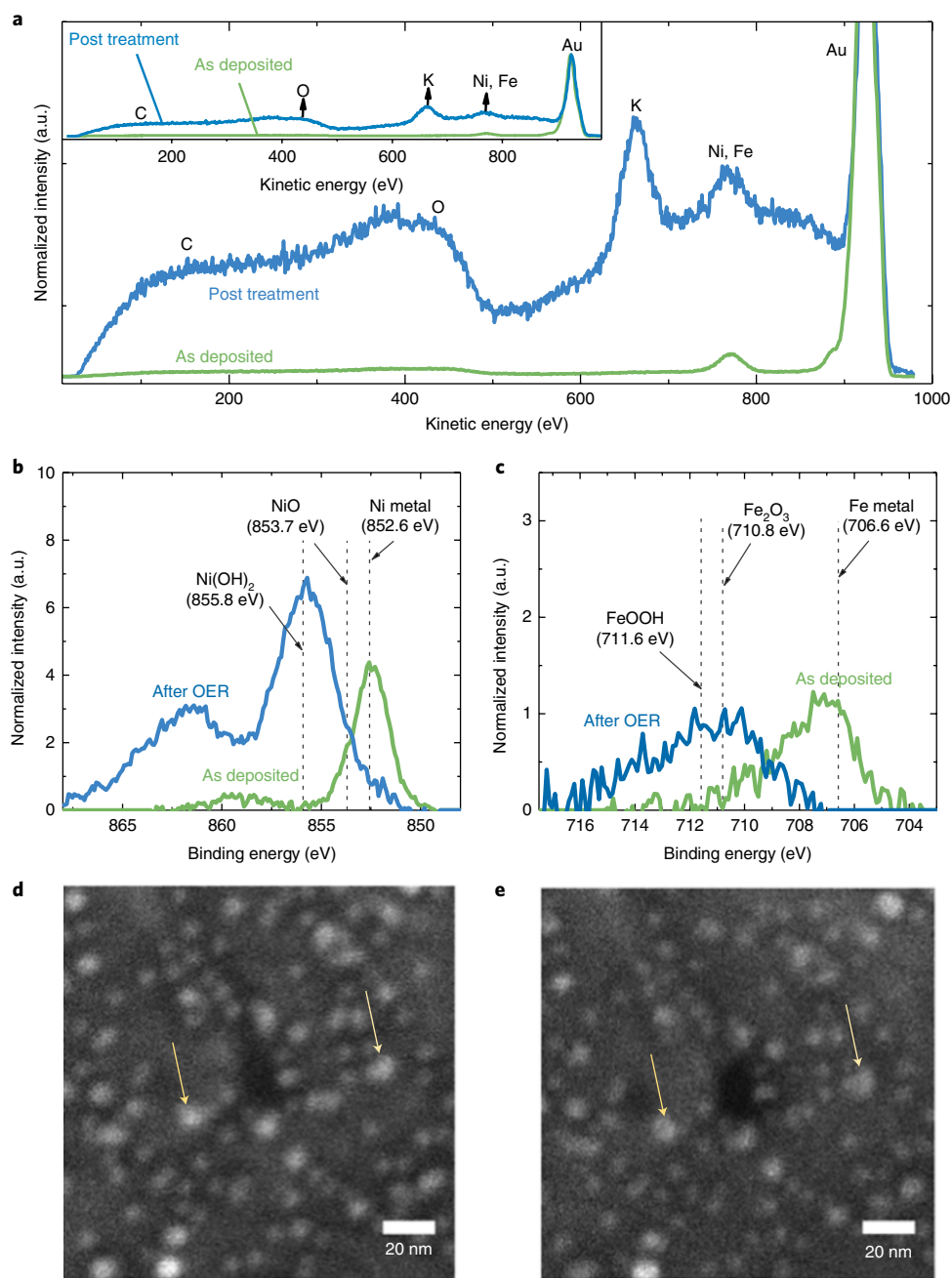


Fig. 2 | Ex situ characterization of the deposited 6.7 nm NiFe particles. **a**, LEIS spectra, **b–e**, XPS spectra (**b,c**) and SEM (**d,e**) of nanoparticles as deposited (**b,d**) and after electrochemical testing (**c,e**). The LEIS spectra are normalized to the height of the Au peak. The XPS spectra, shown for the Ni $2p_{3/2}$ (**b**) and Fe $2p_{3/2}$ (**c**) regions, are charge corrected and normalized with the Au $4f$ peak area after the subtraction of a Shirley background. The reference XPS binding energies are taken from refs ^{59–61}. The SEM images are taken at identical locations to evaluate the resistance against sintering and corrosion.

electrochemical treatment showed that oxide and hydroxide states are formed for both Ni and Fe. More precisely, NiO and Ni(OH)₂, and FeOOH and Fe₂O₃, were identified from the Ni and Fe $2p$ peaks, respectively. The composition determined based on the XPS spectra shows a similar Fe content before the electrochemical testing to the target for the deposition, namely 25%, and an Fe content of ~15% after electrochemical testing for all the nanoparticle sizes (Supplementary Note 3).

One challenge with nanoparticle catalysts is that they often coalesce under reaction conditions^{41–43}. In addition, the conditions under which the OER electrodes operate can cause metal dissolution^{44,45}. As a first step to evaluate the stability and resistance towards

corrosion and sintering, SEM images were acquired before and after the OER at identical locations to visualize directly any change in particle size or positions⁴⁶. From the example images shown in Fig. 2d,e taken before and after testing the activity, it can be seen that the 5.4 nm NiFe particles do not coalesce or dissolve during the two hour potentiostatic measurement at 1.6 V_{RHE}. Most of the nanoparticles can be found directly in both images. To probe the stability further, a chronoamperometric measurement was performed at 1.6 V_{RHE}. As presented in Fig. 3, the OER current was stable over 41 days (~1,000 hours). This result further confirms the stability of the NiFe catalyst previously reported by a stable chronoamperometric measurement at 10 mA cm⁻² over 24 hours^{47,48}.

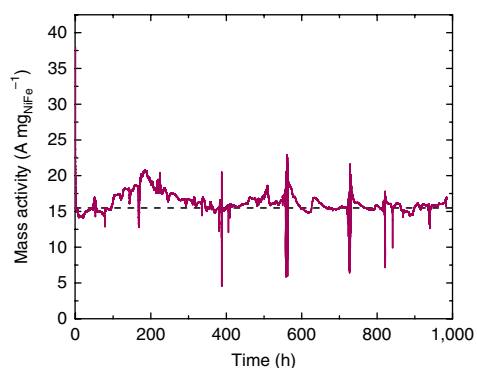


Fig. 3 | Stability of NiFe nanoparticles at 1.6 V_{RHE} in 1M KOH. The mass activity of ~100 ng of 6.7 nm NiFe nanoparticles at 1.6 V_{RHE}, with current interrupt (*iR*) correction, in 1M KOH. The dashed line is a guide to the eye.

To gain insight into the morphology and composition at the atomic level, we acquired identical-location HRTEM images of particles deposited on graphene-covered Au TEM grids both before and after two CV cycles at 10 mV s⁻¹ up to 1.5 V_{RHE}. The electrochemical treatment was mild to avoid the corrosion of the carbon grid at more anodic potentials. Before OER, the NiFe nanoparticles showed a polycrystalline structure. The typical image in Fig. 4a shows a single particle in which the Ni₃Fe phase can be identified⁴⁹. Figure 4b,c shows HRTEM images of the same nanoparticles before and after being electrochemically tested. We found that after electrochemical testing, the nanoparticles maintained their shape and their polycrystalline nature, as indicated by the non-uniform orientation of the lattice fringes, and by the contrast difference caused by diffraction. We used energy-dispersive spectroscopy (EDX) along with a focused electron beam to map the dispersion of Ni and Fe in the particles using cross-sectional line scans (Supplementary Note 4). A comparison of the Ni and Fe concentrations before and after electrochemical testing showed that some of the Fe leaches out after OER. This decrease in Fe concentration could be associated with the dissolution of FeOOH, known to be highly unstable under these experimental conditions⁵⁰.

Activity. The representative CVs of samples from each of the four nanoparticle-size groups, taken after 2 hours at 1.6 V_{RHE}, plotted in Fig. 5a show a clear difference in activity for the different particle sizes. The smallest particles, that is, 3.9 and 5.4 nm, provide the highest current normalized to the deposited metal mass. A significant OER current is observed that starts from $U = -1.5$ V_{RHE} (overpotential of $\eta = 270$ mV). Using what is typically attributed to the Ni²⁺ to Ni^{3+/4+} redox couple¹³, we showed that the integral of the Ni reduction peak scales better with the calculated surface area than the total loading (Supplementary Fig. 4). Less than one electron is transferred per Ni atom in the larger nanoparticles. Figure 5b shows the average mass activity on a deposited metal basis at $\eta = 270$, 300 and 370 mV as a function of particle size. The activity was taken from the current recorded at a scan rate of 10 mV s⁻¹. No obvious difference in trend was observed when comparing the mass activities as a function of the size for different overpotentials.

To show the intrinsic activity, for Fig. 6a we converted the activity into TOF, that is, the number of O₂ molecules produced per active site per unit time, using three estimates for the number of active sites. TOF_{bulk} assumes that all the deposited Ni and Fe atoms are active, TOF_{redox} assumes one active site per electron is transferred in the Ni reduction peak of the CV and TOF_{surface} assumes that only the surface metal atoms of the nanoparticles are active sites (Methods and equations (1)–(6)). We also included the

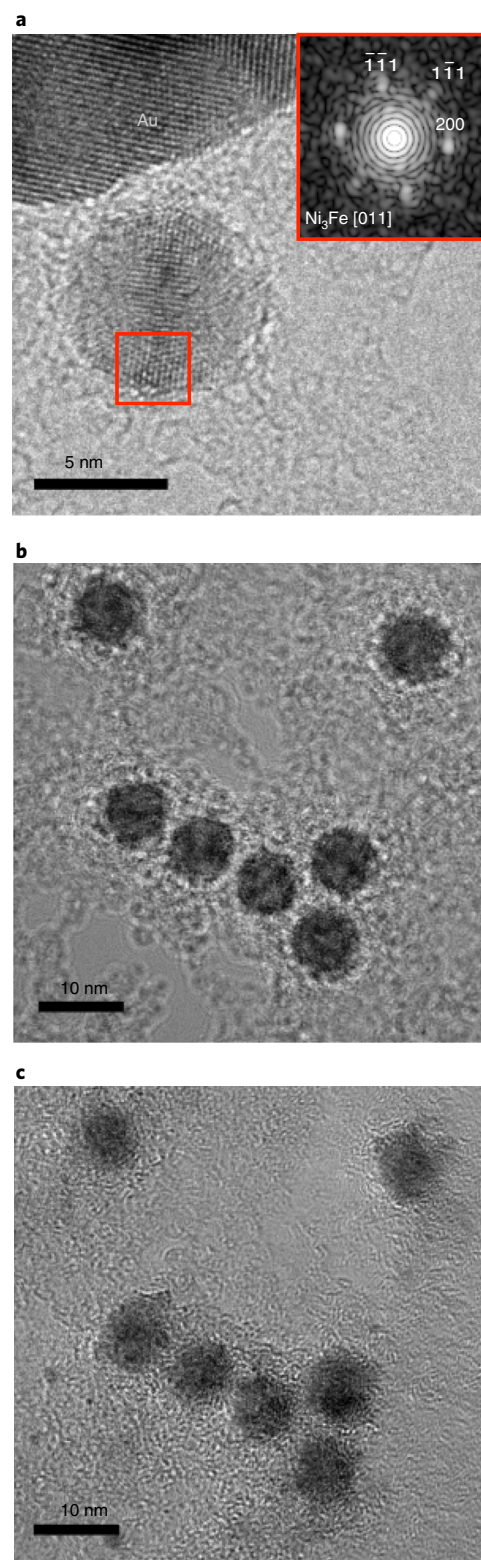


Fig. 4 | HRTEM investigation of the particles. HRTEM images of 6.7 nm (950×10^3 AMU) NiFe nanoparticles deposited on Au TEM grids. **a**, HRTEM image of a nanoparticle. Inset: The Fourier transform of the highlighted area shows the Ni₃Fe phase. **b, c**, Identical-location HRTEM images of nanoparticles before (**b**) and after (**c**) electrochemical oxidation.

TOF_{redox} calculated for NiFeO_xH_y thin films, for which the activity was measured by the same procedure as for the nanoparticles (Supplementary Fig. 5).

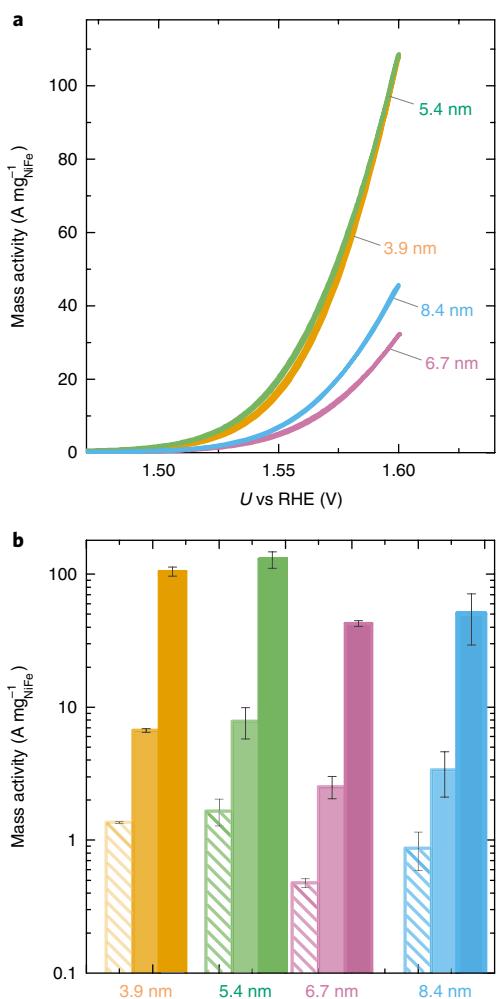


Fig. 5 | Catalytic activity of the NiFe nanoparticles. **a** CV at 10 mV s^{-1} of representative NiFeO_xH_y nanoparticle samples for each nanoparticle size. The current is normalized to the total metal mass loading. **b**, Mass-normalized activities at $\eta = 270$ (hatched), 300 (lighter shade) and 370 mV (darker shade). The average mass activity and s.d. are from three independent samples. All the activity measurements were done on Au substrates in N_2 -saturated 1 M KOH at $1,600$ revolutions per minute. The metal mass was determined from the nanoparticle deposition current.

The TOFs thus calculated show different trends with particle size. TOF_{bulk} is higher for the smaller particles, that is, 5.4 and 3.9 nm , and lower for the larger particles. $\text{TOF}_{\text{redox}}$ and $\text{TOF}_{\text{surface}}$ do not show any obvious particle-size dependence, though $\text{TOF}_{\text{redox}}$ has a larger scatter.

The $\text{TOF}_{\text{surface}}$ and TOF_{bulk} of the 5.4 nm NiFe nanoparticles were compared to state-of-the-art non-noble metal catalysts for the OER in alkaline media (Fig. 6b). The reaction rates of $6.2 \pm 1.6 \text{ s}^{-1}$ ($\text{TOF}_{\text{surface}}$) and $1.2 \pm 0.3 \text{ s}^{-1}$ (TOF_{bulk}) for 5.4 nm NiFe particles at $1.53 \text{ V}_{\text{RHE}}$ ($\eta = 300 \text{ mV}$) are among the highest reported for non-noble metal catalysts in an alkaline electrolyte^{4,16,27,47,51–54}.

Isotope labelling experiments. To provide further insight as to which TOF represents the true intrinsic activity, we used three complementary isotope labelling procedures, all on samples with 6.7 nm particles, referred to below as procedures *a*, *b* and *c*, and illustrated schematically in Fig. 7. The natural oxidation of NiFe particles when exposed to air meant we had to oxidize the catalyst in H_2^{16}O and

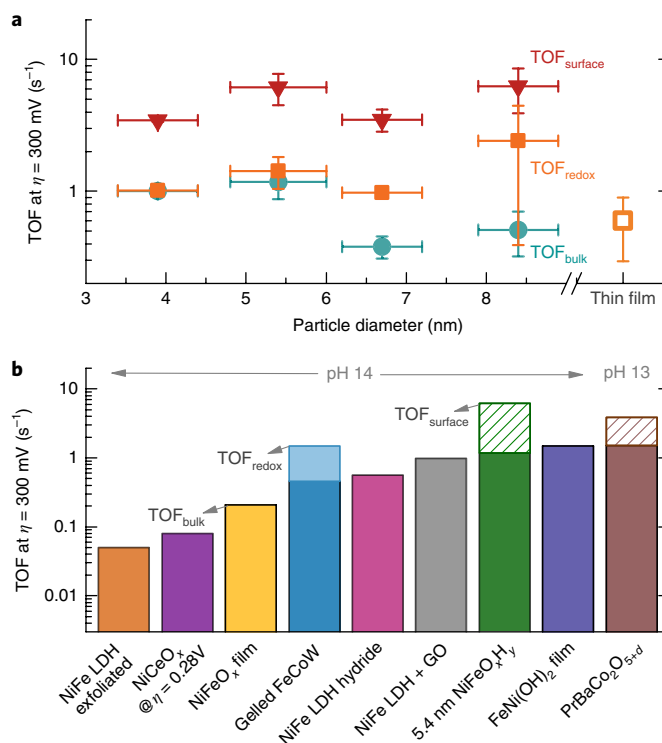


Fig. 6 | TOF as a function of size, and comparison to state-of-the-art non-noble metal catalysts. **a**, TOF calculated from the total metal mass (TOF_{bulk}), the Ni redox peak ($\text{TOF}_{\text{redox}}$) and the estimated surface atoms ($\text{TOF}_{\text{surface}}$) of the NiFe nanoparticles at $\eta = 300 \text{ mV}$ measured in N_2 -saturated 1.0 M KOH at 10 mV s^{-1} as a function of particle size. The Ni redox peak was used to measure the TOF of the NiFe thin film. The y-axis error bars come from three independent samples and were calculated using $\sqrt{\frac{\sum(x-\bar{x})^2}{(n-1)}}$, where x is the activity value and \bar{x} the average activity from the three samples (n). **b**, TOF of state-of-the-art non-noble OER catalysts in alkaline. Sources: NiFe layered double hydroxide (LDH) exfoliated⁵³, NiCeO_x @ $\eta = 0.28 \text{ V}$, NiFeO_x film²⁷, gelled FeCoW (ref. 51), NiFe LDH hydride⁵², NiFe-LDH + GO (ref. 54), $5.4 \text{ nm NiFeO}_x\text{H}_y$ (this work) FeNi(OH)₂ film¹⁶ and $\text{PrBaCo}_2\text{O}_{5+d}$ (ref. 4). When possible, both the minimum (bulk, darker solid colours) and maximum (surface, striped colour, or redox, lighter shade of the solid colour) TOFs were estimated. The $\text{TOF}_{\text{redox}}$ of gelled FeCoW was calculated using the Co redox peak, and the $\text{TOF}_{\text{surface}}$ for $\text{PrBaCo}_2\text{O}_{5+d}$ was calculated based on the surface area from N_2 physisorption (Brunauer-Emmett-Teller).

then perform OER in an ^{18}O -based electrolyte (procedure *a*). We also oxidized the NiFe particles in H_2^{18}O (procedure *b*) and $^{18}\text{O}_2$ (procedure *c*) atmosphere to study the possible differences between hydroxide and oxide compounds.

In procedure *a*, ^{16}O is incorporated into the NiFe nanoparticles through cycling in 0.1 M KOH made from ultrapure water, and the oxygen evolution process takes place in 0.1 M KOH made from ^{18}O water ($\sim 97\% \text{ }^{18}\text{O}$). Due to the natural abundance of ^{16}O , this has the advantage that the nanoparticles can easily be prepared with $99.8\% \text{ }^{16}\text{O}$. However, the lower isotopic purity of ^{18}O -labelled water limits the sensitivity towards isotope exchange of the subsequent EC-MS measurement. In procedures *b* and *c*, ^{18}O is incorporated in the NiFe structure either by cycling in an ^{18}O -labelled 0.1 M KOH electrolyte (procedure *b*) or by heating at $450 \text{ }^\circ\text{C}$ in the vacuum chamber in the presence of $^{18}\text{O}_2$ gas (procedure *c*). This allows for a greater sensitivity towards lattice exchange, but adds some uncertainty to the initial isotopic composition of the catalyst.

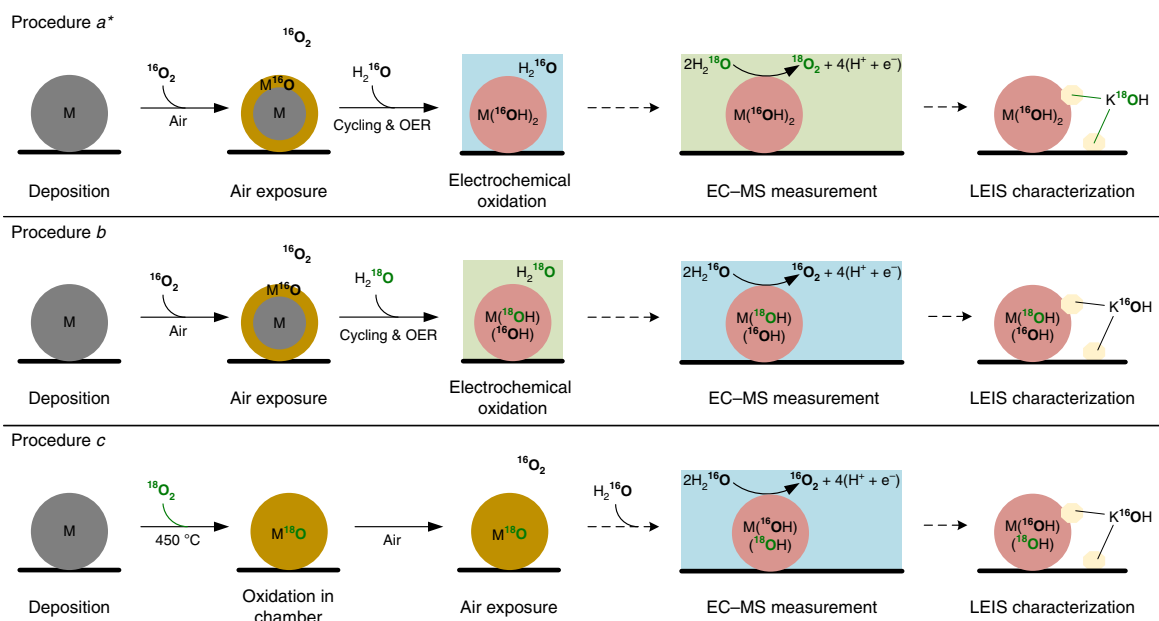


Fig. 7 | Isotope labelling experimental procedures. Schematic representation of the isotopic labelling experiments. Procedure a uses $H_2^{16}O$ to oxidize the nanoparticles and $H_2^{18}O$ for the oxygen evolution, and the opposite is done for Procedure b. Procedure c uses $^{18}O_2$ gas to oxidize NiFe and the oxygen evolution is performed in ^{16}O water. In the representation, M refers to Ni and Fe metal atoms. *The main text focuses on procedure a.

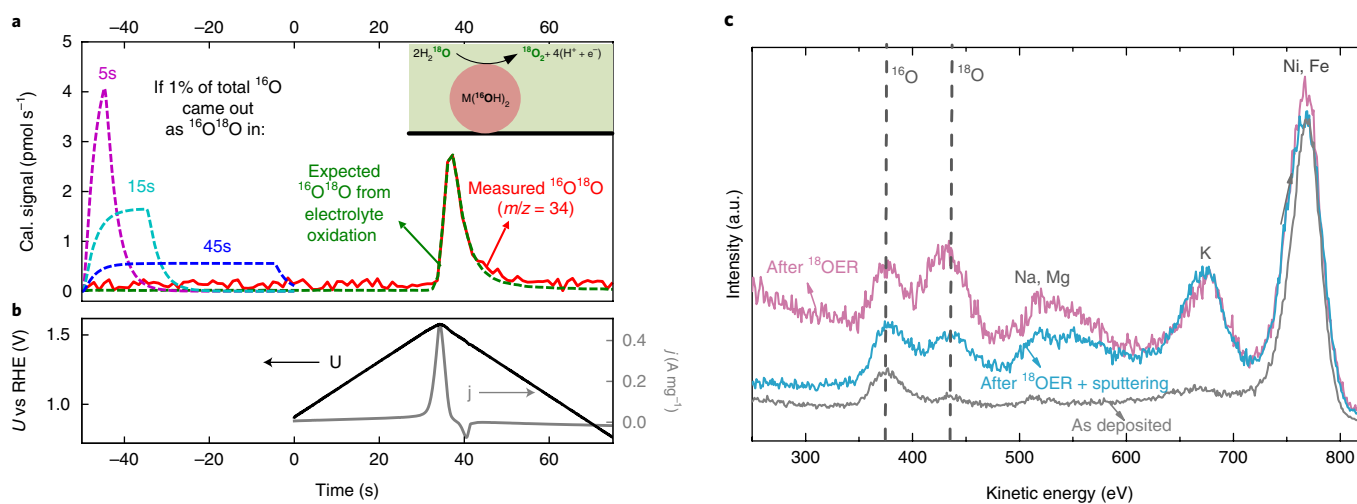


Fig. 8 | EC-MS and LEIS results from the isotope labelling experiment using procedure a. **a**, First linear sweep voltammety in the $H_2^{18}O$ electrolyte after the sample preparation with ^{16}O . Calibrated mass spectrometer signal of $^{16}O^{18}O$ ($m/z = 34$) (red line) detected during oxygen evolution in 0.1 M KOH made with $H_2^{18}O$ during the first electrochemical potential cycle after the sample preparation with ^{16}O . The $^{16}O^{18}O$ signal expected without lattice exchange due to the composition of the electrolyte, which is a constant fraction of the $^{18}O_2$ ($m/z = 36$) signal, is co-plotted (green line). Also included are simulations of the $m/z = 34$ signal if 1% of the total ^{16}O contained by the oxidized catalyst came out as $^{18}O^{16}O$ in 5 s (magenta), 15 s (cyan) or 45 s (blue). The inset is a schematic of the oxygen evolution reaction in a ^{18}O -electrolyte on a $NiFeO_x$ nanoparticle. **b**, The potential (black) and current (grey) from the same experiment. **c**, The LEIS spectra of the sample as deposited (grey), after the EC-MS experiment (purple) and after sputtering (blue).

In procedure a, the sample of deposited particles was cycled in 0.1 M KOH made from ultrapure water until a stable CV was obtained, that is, 20 cycles 0.5–1.5 V_{RHE} . At this point we assumed that the catalyst was in the fully oxygenated form, nominally $M(^{16}OH)_2$ where $M = Ni_xFe_{1-x}$. The electrode was then transferred at an open-circuit voltage to a stagnant thin-layer cell filled with ^{18}O -labelled 0.1 M KOH for measurement by EC-MS. The first cycle up to 1.55 V_{RHE} and back to 0.5 V_{RHE} is shown in Fig. 8a,b. In Fig. 8a, the calibrated $m/z = 34$ ($^{16}O^{18}O$) mass spectrometer signal is plotted

as a function of time, and in Fig. 8b the potential and current are plotted on the same time axis. Co-plotted with the measured $^{16}O^{18}O$ signal in Fig. 8a is the expected $^{16}O^{18}O$ signal due to oxidation of the electrolyte, which contains only $\sim 97\%$ ^{18}O . The expected $^{16}O^{18}O$ signal is the measured $^{18}O_2$ ($m/z = 36$) signal multiplied by the steady-state $^{16}O^{18}O/^{18}O_2$ ratio. This ratio, as well as the calibration, were determined under operando conditions by steady-state oxygen evolution (Supplementary Note 5). The measured and expected $^{16}O^{18}O$ coincided, which indicates that all of the signal at $m/z = 34$

can be explained by the oxidation of the electrolyte alone. The onset of the oxygen signal is delayed with respect to the onset of the OER current by about ~3 s, as predicted by the mass-transport model described in Trimarco et al.³⁸, which indicates that the current at low overpotential does, indeed, go to OER and not another process.

To illustrate the sensitivity, we included in Fig. 8a the expected excess $m/z=34$ signal if 1% of the total ^{16}O contained by the catalyst, equivalent to approximately 10% of a monolayer, were released as $^{16}\text{O}^{18}\text{O}$. The release of 1% of the total ^{16}O in 45 seconds (dashed blue line in Fig. 8a), which corresponds to approximately 0.2% of a monolayer per second, is significantly above the detection limit. In comparison, the peak oxygen signal (at $m/z=36$) in this scan corresponds to 19% of a monolayer per second, or about 100 times greater. This proves that if even 1% of the OER activity were due to lattice oxygen evolution, it would be detectable.

The results of procedures *b* and *c* (Supplementary Fig. 7a–d) are similar, but because of low natural abundance of ^{18}O (0.02%), the sensitivity towards isotope exchange at $m/z=34$ and 36 is even higher. To determine whether the result is general, we also performed the isotope experiment (following procedure *a*) on a NiFeO_xH_y thin film, and again observed no lattice exchange (Supplementary Fig. 7e). Additionally, to prove that our set-up is, indeed, sensitive enough to detect a lattice exchange when it does take place, we performed the same experiment on IrO_2/Ti in acid, as described in Fierro et al.³⁰, and reproduced their result of an isotope exchange greater than one monolayer. In Supplementary Fig. 8, this result is directly compared with that from NiFeO_xH_y .

In procedure *a*, after the EC–MS, the sample was rinsed in H_2^{18}O before being transferred back to a vacuum for LEIS. The LEIS spectrum after OER, that is, the purple line in Fig. 8c, shows additional peaks when compared to the initial LEIS spectrum (black line), which we attribute to ^{16}O , ^{18}O , impurity Na and Mg salt deposits from the H_2^{18}O rinsing, and to residual K from the electrolyte. The sample was then Ar-sputtered for 30 minutes before another LEIS spectrum was taken. This spectrum (blue line) shows an increased $^{16}\text{O}/^{18}\text{O}$ ratio, compared to the initial one. We therefore attribute the ^{18}O peak to residual K^{18}OH and/or other hydroxide salts on the surface of the sample and the ^{16}O peak to ^{16}O that remained in the catalyst. After both procedures *b* and *c*, the $^{18}\text{O}/^{16}\text{O}$ ratio in LEIS after OER, rinsing with ultrapure water and sputtering, was approximately 1:1, with little to no K or other impurities, as shown in Supplementary Fig. 7. In both cases, there is a clear ^{18}O signal even before sputtering, which indicates that this isotope is present at the surface of the catalyst. The postsputtering 1:1 ratio presumably reflects the nominal $\text{M}^{(18}\text{OH})(^{16}\text{OH})$ formula that results from the experimental procedures, as illustrated in Fig. 7b,c. As the natural abundance of ^{18}O is so low (0.2%), the presence of ^{18}O on the LEIS spectra in procedures *b* and *c* implies that it was incorporated during the catalyst preparation before OER, and not during transfer through air from EC–MS to LEIS.

Discussion

The results obtained from the identical-location SEM (Fig. 2c), in addition to the stable current over 1,000 hours (Fig. 3), prove that the NiFeO_xH_y particles are remarkably stable against corrosion.

The activity dependence on particle size is similar at 270, 300 and 370 mV overpotential (Fig. 5b). This is consistent with a lack of subsurface activity, which would involve the diffusion of water and oxygen through the nanoparticles, and could therefore introduce greater mass transport limitations for larger particles at high overpotentials, if the diffusion is sufficiently slow. Furthermore, the activity of the particles normalized to surface area, that is, $\text{TOF}_{\text{surface}}$, does not change with particle size (Fig. 6a). In contrast, the activity of the particles normalized to the total mass, which is proportional to the TOF_{bulk} , decreases with increasing particle size. Different Fe content cannot explain the observed trends (Supplementary Fig. 2b).

$\text{TOF}_{\text{redox}}$ of the electrodeposited NiFeO_xH_y film shows a similar activity to that reported by Trotochaud et al.²⁷. This is slightly lower than the $\text{TOF}_{\text{redox}}$ for the nanoparticles, also consistent with a lack of subsurface activity and the observation that the Ni redox peak probes more than the Ni surface atoms.

Mass spectrometry and LEIS measurements for isotope experiments on NiFeO_xH_y particles using three different approaches all indicate that oxygen is retained in the catalyst during OER, both in the bulk and, to at least some degree, also on the surface of the catalyst. Isotope experiments on a NiFeO_xH_y thin film agree. The significance of this result is twofold. First, it provides additional evidence against activity below the outer surface or a near-surface region in which water is highly mobile, as this would involve lattice oxidation and/or the oxidation of low-mobility intercalated water. Second, the oxygen evolution mechanism does not proceed via lattice oxygen.

Based on the arguments above, we conclude that active sites are limited to a near-surface region, and that $\text{TOF}_{\text{redox}}$ is a lower bound to the intrinsic activity of the active sites. Previous studies that show a linear correlation between loading and activity used porous electrodes without a well-defined outer surface²⁴. Given the evidence presented here against bulk activity, we explain this observation on the basis that the surface area scales linearly with loading for these porous materials.

However, to determine if activity is limited to the outer surface atomic layer ($\text{TOF}_{\text{surface}}$) is more difficult. Although the charge passed in the Ni redox feature during cyclic voltammetry corresponds to ~3 atomic layers, this does not necessarily mean that this entire region also participates in OER. The nature of the transport involved in the Ni redox feature in alkaline is an unsolved problem¹³, and models based on the transport of protons, hydroxide or cations have been proposed⁵⁵. Whereas the Ni redox feature may only require the shuttling of a proton, OER necessarily requires the net transport of oxygen species. Our isotope result indicates that transport below the outer surface is either so slow as to inhibit OER or fast enough that any water or hydroxide in this region exchanges with the electrolyte before the onset of OER. We must admit that we cannot yet conclusively distinguish between the two possibilities.

As mentioned previously, lattice exchange is material dependent. The phenomenon is observed with Co_3O_4 (ref. 31), iridium-based catalysts³⁰ and a few perovskites³⁴. Besides being sensitive to the composition of the material, the lattice oxygen exchange also seems to be dependent on the structure. Indeed, lattice exchange was observed with amorphous and nanocrystalline RuO_2 phases with undercoordinated edge sites^{28,33}, but not with crystalline rutile RuO_2 (ref. 36). Although we did not observe lattice exchange during OER in the case of NiFeO_xH_y nanoparticles or an electrodeposited NiFeO_xH_y thin film, the results may not be generalizable to all synthesis methods. Furthermore, we cannot rule out that such phenomena could, in principle, occur at much higher potentials which, unfortunately, cannot yet be studied in our EC–MS set-up, due to bubble formation.

The absence of the participation of lattice oxygen in NiFeO_xH_y , is in disagreement with the hypothesis that lattice exchange should occur with materials that have a catalytic activity that is pH dependent on the hydrogen scale³⁴, which is the case for NiFeO_xH_y (ref. 56). In contrast, it provides evidence for an associative mechanism, such as that proposed by Bell and co-workers¹⁹.

In summary, we used well-characterized mass-selected nanoparticles of Ni and Fe as a model system to investigate their fundamental properties under oxygen-evolution conditions. We provided fundamental insight into the reaction and the origin of the high performance using LEIS spectroscopy and the microchip-based EC–MS set-up. The particles showed an exceptionally high activity and stability over 1,000 hours at 1.6 V_{RHE} . Isotope-labelling experiments performed after three distinct approaches showed that there was no participation of lattice oxygen or intercalated water in the oxygen

evolution. This allows us to conclude that the active sites responsible for such exceptional activity are only located in the ~3 atomic layer redox-active near-surface region of the nanoparticles, but to determine if the activity is limited to the outer surface requires a better knowledge of the ionic transport mechanisms within this region. Normalizing the activity to the outer surface results in a TOF of $6.2 \pm 1.6 \text{ s}^{-1}$ at $\eta = 0.3 \text{ V}$, the highest reported to date. Further enhancements to the catalytic activity should focus on tailoring the atoms at the near-surface region, as opposed to the bulk.

Methods

Preparation of mass-selected NiFe nanoparticles. NiFe nanoparticles were prepared using a noble-gas aggregation magnetron sputtering nanoparticle source combined with a lateral time-of-flight mass filter (Fig. 1a) capable of mass selection of the nanoparticles before deposition³⁷ (Nano-Beam 2011, Birmingham Instruments Ltd) similar to that described by Pratontep et al.³⁸. A 75 at% Ni/25 at% Fe sputtering target (99.95%, Kurt J. Lesker Ltd) was used and the particles were deposited onto clean and smooth Au disks. The nanoparticle source was fully UHV compatible and the mass filter had a base pressure in the low 10^{-10} mbar region. The mass filter was set to be used with negatively charged particles, and to have a mass resolution of $\sim m/\Delta m = 20$ to maximize the current of the particles. The vast majority of the particles that exited the nanoparticle source carried a single charge, and thus the current measured on the sample during the deposition together with the deposition time can be translated into the number of deposited particles. If not otherwise stated, the loading of the electrodes was a 15% projected surface area coverage, which corresponds to a total metal mass loading of 50–125 ng, which means a 315–785 ng cm^{-2} loading in circular spots of 4.5 mm in diameter, depending on the particle size.

Determination of particle-size distributions. NiFe nanoparticles with masses of 120,000, 350,000, 950,000 and 2,000,000 AMU were deposited onto Cu TEM grids covered with lacey carbon (300 mesh, Agar Scientific Ltd). After deposition and transfer under atmospheric conditions, the particles were imaged in the bright-field TEM mode in an FEI Tecnai T20 G² equipped with a thermionic electron source and using a 200 keV acceleration voltage. The images were analysed with ImageJ software to extract the average area of the particle projections, and a diameter was calculated assuming a circular shape (Supplementary Note 1).

Electrochemical measurements. Electrochemical measurements were performed using a rotating disk electrode in a PTFE (Teflon) cell at 1,600 revolutions per minute in N_2 -saturated 1.0 M KOH. A carbon rod was used as the counter electrode with a Hg/HgO electrode as the reference electrode, which was calibrated to the RHE in the same electrolyte saturated with 1 bar H_2 over a clean Pt mesh before each experiment. The Ohmic drop was measured by using electrochemical impedance spectroscopy over a range of 10–200,000 Hz at an a.c. amplitude of 10 mV. The high-frequency intercept was fitted to an equivalent circuit to obtain the Ohmic losses, which typically ranged from 4 to 18 Ω . The Ohmic drop compensation was done by online Ohmic drop correction in which an 85% correction was applied. Ultrapure water (Milli-Q, 18.2 M Ω cm) with KOH (semiconductor grade, pellets, 99.9%) were used to prepare 1.0 M KOH. The initial catalytic activity was measured by recording five cyclic voltammograms at 10 mV s^{-1} up to 1.6 V_{RHE} followed by a 2 h potentiostatic measurement at 1.6 V_{RHE}. Finally, the activity was again assessed using CV. The activity of the different samples for the OER presented in this work was taken from the final CV. For each experiment, three independent samples were tested and the activity was averaged (Supplementary Figs. 9–11). The longer stability measurement was a static measurement at 1.6 V_{RHE}, for which the NiFe particles were deposited onto a gold sheet. The duration of this experiment meant only two samples were tested. The mass activity was obtained by normalizing the current with the total mass of Ni and Fe determined from the deposition current and time.

To compare the differences between lattice oxygen participation in NiFeO_xH_y nanoparticles and thin film, thin films of NiFeO_xH_y were electrodeposited. Using a three-electrode set-up, a current of -0.2 mA cm^{-2} for 5 min in an electrolyte of 0.1 M Ni(NO₃)₂·6H₂O and 5 mM FeCl₂. The composition determined by XPS indicates a mixture of approximately 32% Fe and 68% Ni at the surface.

Turnover frequency. To calculate the TOF, we used the formula:

$$\text{TOF} (\text{s}^{-1}) = \frac{r_{\text{O}_2}}{\text{of active sites}} \quad (1)$$

The rate of O₂ turnovers ($r_{\text{O}_2} \text{ s}^{-1}$) was calculated from the raw current:

$$r_{\text{O}_2} = i \times \left(\frac{N_A}{zF} \right) \quad (2)$$

Where i (A) is the current, N_A is the Avogadro number (6.022×10^{23} O₂ molecules per mol O₂), z is the number of electrons involved in the evolution of 1 O₂ molecule and F the Faraday constant (96,485 C mol⁻¹).

We determined a minimum (TOF_{bulk}) and a maximum (TOF_{surface}) TOF based on two different assumptions on the number of active sites.

For the calculation of TOF_{bulk}, we assumed that all the metal atoms deposited are active for OER. To calculate the total number of Ni and Fe metal atoms deposited on the surface ($N_{\text{metal atom}}^{\text{total}}$), the number of deposited particles ($N_{\text{particles}}^{\text{metal}}$) were multiplied by the average number of atoms in each particle ($N_{\text{metal atom}}^{\text{particle}}$):

$$N_{\text{metal atom}}^{\text{total}} = N_{\text{particles}} \times N_{\text{metal atom}}^{\text{particle}} \quad (3)$$

$N_{\text{particles}}$ can be calculated from the deposition current (I_{depo} (A)), time of deposition (t_{depo} (s)) and the electric charge C (6.242×10^{-18} electrons C⁻¹) using equation (4):

$$N_{\text{particles}} = I_{\text{depo}} \times t_{\text{depo}} \times C \quad (4)$$

Finally, to calculate the number of metal atoms in a particle, we used the deposited particle mass set by the mass filter (m_{particle} (kg)), N_A (mol⁻¹) and the average molar mass ($M_{\text{Ni}_x\text{Fe}_{1-x}}$ [kgmol⁻¹]) using the composition determined from the XPS after electrochemical treatment for each sample:

$$N_{\text{metal atom}}^{\text{particle}} = \frac{N_A \times m_{\text{particle}}}{M_{\text{Ni}_x\text{Fe}_{1-x}}} \quad (5)$$

To calculate the TOF_{surface}, the number of surface Ni and Fe atoms had to be calculated. The diameter of the nanoparticles was determined by TEM images and used to calculate the surface area per particle (A_{particle}) assuming a spherical shape. This is a conservative approach as part of the nanoparticle's surface will interface with the substrate and therefore will not contribute to the OER. Finally, this area was multiplied by $N_{\text{particles}}$ and the density of surface metal atoms to get the total number of surface Ni and Fe atoms. The assumed density of the surface metal atoms (ρ_{atoms}) of 12.5 metal atoms nm⁻² is based on the metal–metal distance of 2.83 Å for NiFeO_xH_y measured in situ under OER conditions¹⁹:

$$N_{\text{surface atom}}^{\text{total}} = N_{\text{particles}} \times \rho_{\text{atoms}} \times A_{\text{particle}} \quad (6)$$

XPS and LEIS characterization. LEIS (Supplementary Figs. 12 and 13) and XPS spectra (Supplementary Figs. 14–16) were recorded for each sample after deposition (without breaking the vacuum) and after activity testing. To remove the remaining electrolyte on the surface after the activity test, the samples were thoroughly rinsed with ultrapure water (18.2 M Ω cm) before loading into the ultrahigh vacuum chamber to prevent the formation of a potassium layer hindering the detection of other elements.

For LEIS measurements, 1 keV He⁺ ions from an Omicron ISE100 ion gun were used and the energy of the scattered ions was recorded with the same 7-channel analyser used for XPS measurements operated in constant retard ratio mode (with a retard ratio of 5). The LEIS spectra presented are normalized based on the intensity of the gold peak at ~ 925 eV.

For the XPS measurements, unmonochromatized Mg K α radiation from a SPECS XR50 dual filament X-ray gun was used. The electron energies were measured with an Omicron NanoSAM 7-channel energy analyser operated in the constant pass energy mode. A pass energy of 50 eV was chosen to increase the signal from the low loadings of nanoparticles. For each sample, a survey scan and detailed scans of Au 4f, O 1s, Ni 2p_{3/2} and Fe 2p_{3/2} were recorded. All the spectra were charge corrected based on the Au 4f_{7/2} peak, which we assumed to correspond to metallic Au at 84 eV binding energy. A Shirley background was subtracted from the detailed spectra presented and the intensities were normalized with the Au 4f peak area.

Identical-location SEM imaging. Identical-location SEM imaging was performed on a sample that contained 5.4 nm NiFe particles on the Au electrode after deposition and transfer under atmospheric conditions and after electrochemical testing. SEM images were acquired at 5 kV using an FEI Helios EBS3 microscope equipped with a field emission gun and a through-the-lens detector for high-resolution imaging.

Identical-location TEM imaging and EDX line scans. Identical-location HRTEM images were recorded at 80 kV electron energy, using a FEI Titan E-Cell 80–300 ST TEM with a monochromated electron source and postobjective aberration correction. For the identical-location TEM studies, particles were deposited on Au-coated Cu TEM grids with suspended monolayer graphene layers (Quantifoil). After imaging, the grids were mounted to a rotating disk electrode set-up and subjected to two CVs at 10 mV s^{-1} between 1 and 1.5 V_{RHE} in 1 M KOH. After the electrochemical oxidation, the particles were transferred back to the TEM and imaged a second time. EDX line scans were recorded using a silicon drift detector from Oxford Instruments on random particles before and after electrochemical oxidation.

EC–MS experiments. To investigate oxygen exchange between the NiFe particles and the electrolyte, isotopically labelled electrolyte (with ¹⁸O) and EC–MS were used. The EC–MS set-up was based on a microfabricated membrane coated with

a fluorinated polymer and a well-defined capillary. Below the membrane, a small cavity was pressurized with He carrier gas and, together with the capillary forces, the electrolyte is kept out of the chip. The cavity was connected to a vacuum chamber equipped with a quadrupole mass spectrometer (Pfeiffer Vacuum QMA 125) through a well-defined microfabricated capillary that limited the flow of molecules to a level that can be handled by a single turbomolecular pump. For the experiments, a self-designed stagnant layer electrochemical cell was used in which the electrolyte thickness was 100 μm , which, together with the design of the vacuum chamber and microchip, gave a time response below 1 s. The area under the modelled curves in Fig. 8 (blue, magenta and cyan lines) corresponds to the nominal number labelled oxygen atom in the nanoparticle samples, and the shapes of these curves were calculated by a mass transport model that accounted for diffusion of O_2 through the 100 μm electrolyte layer. Details of the set-up, experimental method and mass-transport model are described elsewhere³⁸. All the experiments were performed using a 0.1 M KOH electrolyte made with either ultrapure water (natural isotope distribution) or ^{18}O enriched water (97.2% H_2^{18}O , 1.3% H_2^{17}O and 1.5% H_2^{16}O , Medical Isotopes). The mass spectrometer signals were calibrated internally for each experiment, as was the steady-state ratio of $m/z = 34$ to $m/z = 36$ for procedure a. The raw data for these calibrations are shown (for procedure a) in Supplementary Fig. 6.

Data availability

The data that support the plots within this paper and other findings of this study are available from the corresponding author upon reasonable request.

Received: 28 February 2018; Accepted: 14 September 2018;

Published online: 5 November 2018

References

- Lewis, N. S. & Nocera, D. G. Powering the planet: chemical challenges in solar energy utilization. *Proc. Natl Acad. Sci. USA* **103**, 15729–15735 (2006).
- Debe, M. K. Electrocatalyst approaches and challenges for automotive fuel cells. *Nature* **486**, 43–51 (2012).
- Montoya, J. H. et al. Materials for solar fuels and chemicals. *Nat. Mater.* **16**, 70–81 (2017).
- Hong, W. T. et al. Toward the rational design of non-precious transition metal oxides for oxygen electrocatalysis. *Energy Environ. Sci.* **8**, 1404–1427 (2015).
- Durst, J. et al. New insights into the electrochemical hydrogen oxidation and evolution reaction mechanism. *Energy Environ. Sci.* **7**, 2255–2260 (2014).
- Stamenkovic, V. R., Strmcnik, D., Lopes, P. P. & Markovic, N. M. Energy and fuels from electrochemical interfaces. *Nat. Mater.* **16**, 57–69 (2017).
- Greeley, J. & Markovic, N. M. The road from animal electricity to green energy: combining experiment and theory in electrocatalysis. *Energy Environ. Sci.* **5**, 9246 (2012).
- Cifrain, M. & Kordesch, K. in *Handbook of Fuel Cells—Fundamentals, Technology and Applications* Vol. 1 (eds Vielstich, W.A., Gasteiger, H.A. & Lamm, A.) 267–280 (Wiley, Hoboken, 2010).
- Pagliari, M., Konstandopoulos, A. G., Ciriminna, R. & Palmisano, G. Solar hydrogen: fuel of the near future. *Energy Environ. Sci.* **3**, 279 (2010).
- Seh, Z. W. et al. Combining theory and experiment in electrocatalysis: insights into materials design. *Science* **355**, eaad4998 (2017).
- The production of hydrogen and oxygen through the electrolysis of water. *Scientific American Supplement* No. 819 Vol. XXXII, article II (1891).
- Trotochaud, L., Young, S. L., Ranney, J. K. & Boettcher, S. W. Nickel–iron oxyhydroxide oxygen-evolution electrocatalysts: the role of intentional and incidental iron incorporation. *J. Am. Chem. Soc.* **136**, 6744–6753 (2014).
- Dionigi, F. & Strasser, P. NiFe-based (oxy)hydroxide catalysts for oxygen evolution reaction in non-acidic electrolytes. *Adv. Energy Mater.* **6**, 1600621 (2016).
- Burke, M. S., Enman, L. J., Batchellor, A. S., Zou, S. & Boettcher, S. W. Oxygen evolution reaction electrocatalysis on transition metal oxides and (oxy)hydroxides: activity trends and design principles. *Chem. Mater.* **27**, 7549–7558 (2015).
- Enman, L. J., Burke, M. S., Batchellor, A. S. & Boettcher, S. W. Effects of intentionally incorporated metal cations on the oxygen evolution electrocatalytic activity of nickel (oxy)hydroxide in alkaline media. *ACS Catal.* **6**, 2416–2423 (2016).
- Klaus, S., Cai, Y., Louie, M. W., Trotochaud, L. & Bell, A. T. Effects of Fe electrolyte impurities on $\text{Ni}(\text{OH})_2/\text{NiOOH}$ structure and oxygen evolution activity. *J. Phys. Chem. C* **119**, 7243–7254 (2015).
- Li, N. et al. Influence of iron doping on tetravalent nickel content in catalytic oxygen evolving films. *Proc. Natl Acad. Sci. USA* **114**, 1486–1491 (2017).
- Görlin, M. et al. Oxygen evolution reaction dynamics, Faradaic charge efficiency, and the active metal redox states of Ni–Fe oxide water splitting electrocatalysts. *J. Am. Chem. Soc.* **138**, 5603–5614 (2016).
- Friebel, D. et al. Identification of highly active Fe sites in $(\text{Ni,Fe})\text{OOH}$ for electrocatalytic water splitting. *J. Am. Chem. Soc.* **137**, 1305–1313 (2015).
- Stevens, M. B., Trang, C. D. M., Enman, L. J., Deng, J. & Boettcher, S. W. Reactive Fe-Sites in Ni/Fe (oxy)hydroxide are responsible for exceptional oxygen electrocatalysis activity. *J. Am. Chem. Soc.* **139**, 11361–11364 (2017).
- Hunter, B., Winkler, J. & Gray, H. Iron is the active site in nickel/iron water oxidation electrocatalysts. *Molecules* **23**, 903 (2018).
- Ahn, H. S. & Bard, A. J. Surface interrogation scanning electrochemical microscopy of $\text{Ni}_{1-x}\text{Fe}_x\text{OOH}$ ($0 < x < 0.27$) oxygen evolving catalyst: kinetics of the ‘fast’ iron sites. *J. Am. Chem. Soc.* **138**, 313–318 (2016).
- Xiao, H., Shin, H. & Goddard, W. A. Synergy between Fe and Ni in the optimal performance of $(\text{Ni,Fe})\text{OOH}$ catalysts for the oxygen evolution reaction. *Proc. Natl Acad. Sci. USA* **115**, 5872–5877 (2018).
- Batchellor, A. S. & Boettcher, S. W. Pulse-electrodeposited Ni–Fe (oxy) hydroxide oxygen evolution electrocatalysts with high geometric and intrinsic activities at large mass loadings. *ACS Catal.* **5**, 6680–6689 (2015).
- Doyle, A. D., Bajdich, M. & Vojvodica, A. Theoretical insights to bulk activity towards oxygen evolution in oxyhydroxides. *Catal. Lett.* **147**, 1533–1539 (2017).
- Morales-Guio, C. G., Liardet, L. & Hu, X. Oxidatively electrodeposited thin-film transition metal (oxy)hydroxides as oxygen evolution catalysts. *J. Am. Chem. Soc.* **138**, 8946–8957 (2016).
- Trotochaud, L., Ranney, J. K., Williams, K. N. & Boettcher, S. W. Solution-cast metal oxide thin film electrocatalysts for oxygen evolution. *J. Am. Chem. Soc.* **134**, 17253–17261 (2012).
- Wohlfahrt-Mehrens, M. & Heitbaum, J. Oxygen evolution on Ru and RuO_2 electrodes studied using isotope labelling and on-line mass spectrometry. *J. Electroanal. Chem. Interfacial Electrochem.* **237**, 251–260 (1987).
- Diaz-Morales, O., Calle-Vallejo, F., de Munck, C. & Koper, M. T. M. Electrochemical water splitting by gold: evidence for an oxide decomposition mechanism. *Chem. Sci.* **4**, 2334 (2013).
- Fierro, S., Nagel, T., Baltruschat, H. & Cominellis, C. Investigation of the oxygen evolution reaction on Ti/ IrO_2 electrodes using isotope labelling and on-line mass spectrometry. *Electrochem. Commun.* **9**, 1969–1974 (2007).
- Amin, H. M. A. & Baltruschat, H. How many surface atoms in Co_3O_4 take part in oxygen evolution? Isotope labeling together with differential electrochemical mass spectrometry. *Phys. Chem. Chem. Phys.* **19**, 25527–25536 (2017).
- Surendranath, Y., Kanan, M. W. & Nocera, D. G. Mechanistic studies of the oxygen evolution reaction by a cobalt–phosphate catalyst at neutral pH. *J. Am. Chem. Soc.* **132**, 16501–16509 (2010).
- Macounova, K., Makarova, M. & Krtil, P. Oxygen evolution on nanocrystalline RuO_2 and $\text{Ru}_0.9\text{Ni}_{0.1}\text{O}_{2-x}$ electrodes—DEMS approach to reaction mechanism determination. *Electrochem. Commun.* **11**, 1865–1868 (2009).
- Grimaud, A. et al. Activating lattice oxygen redox reactions in metal oxides to catalyse oxygen evolution. *Nat. Chem.* **9**, 457–465 (2017).
- Willsau, J., Wolter, O. & Heitbaum, J. In the oxygen evolution reaction on platinum? *J. Electroanal. Chem.* **195**, 299–306 (1985).
- Stoerzinger, K. A. et al. Orientation-dependent oxygen evolution on RuO_2 without lattice exchange. *ACS Energy Lett.* **2**, 876–881 (2017).
- Lu, X. & Zhao, C. Electrodeposition of hierarchically structured three-dimensional nickel–iron electrodes for efficient oxygen evolution at high current densities. *Nat. Commun.* **6**, 6616 (2015).
- Trimarco, D. B. et al. Enabling real-time detection of electrochemical desorption phenomena with sub-monolayer sensitivity. *Electrochim. Acta* **268**, 520–530 (2018).
- Paoli, E. A. et al. Oxygen evolution on well-characterized mass-selected Ru and RuO_2 nanoparticles. *Chem. Sci.* **6**, 190–196 (2015).
- Li, Z. Y. et al. Three-dimensional atomic-scale structure of size-selected gold nanoclusters. *Nature* **451**, 46–48 (2008).
- Ferreira, P. J. et al. Instability of Pt/C electrocatalysts in proton exchange membrane fuel cells. *J. Electrochem. Soc.* **152**, A2256 (2005).
- Meier, J. C. et al. Design criteria for stable Pt/C fuel cell catalysts. *Beilstein J. Nanotechnol.* **5**, 44–67 (2014).
- Fiordaliso, E. M., Dahl, S. & Chorkendorff, I. Strong metal support interaction of Pt and Ru nanoparticles deposited on HOPG probed by the H–D exchange reaction. *J. Phys. Chem. C* **116**, 5773–5780 (2012).
- Binninger, T. et al. Thermodynamic explanation of the universal correlation between oxygen evolution activity and corrosion of oxide catalysts. *Sci. Rep.* **5**, 12167 (2015).
- Spöri, C., Kwan, J. T. H., Bonakdarpour, A., Wilkinson, D. P. & Strasser, P. The stability challenges of oxygen evolving catalysts: towards a common fundamental understanding and mitigation of catalyst degradation. *Angew. Chem. Int. Ed.* **56**, 5994–6021 (2017).
- Hartl, K., Hanzlik, M. & Arenz, M. IL-TEM investigations on the degradation mechanism of Pt/C electrocatalysts with different carbon supports. *Energy Environ. Sci.* **4**, 234–238 (2011).
- Ng, J. W. D. et al. Gold-supported cerium-doped NiO_x catalysts for water oxidation. *Nat. Energy* **1**, 16053 (2016).
- Xu, X., Song, F. & Hu, X. A nickel iron diselenide-derived efficient oxygen-evolution catalyst. *Nat. Commun.* **7**, 12324 (2016).

49. Silva, H. et al. Synthesis and characterization of Fe-Ni/ γ -Al₂O₃ egg-shell catalyst for H₂ generation by ammonia decomposition. *Appl. Catal. A* **505**, 548–556 (2015).
50. Burke, M. S. et al. Revised oxygen evolution reaction activity trends for first-row transition-metal (oxy)hydroxides in alkaline media. *J. Phys. Chem. Lett.* **6**, 3737–3742 (2015).
51. Zhang, B. et al. Homogeneously dispersed multimetal oxygen-evolving catalysts. *Science* **352**, 333–337 (2016).
52. Gong, M. et al. An advanced Ni-Fe layered double hydroxide electrocatalyst for water oxidation. *J. Am. Chem. Soc.* **135**, 8452–8455 (2013).
53. Song, F. & Hu, X. Exfoliation of layered double hydroxides for enhanced oxygen evolution catalysis. *Nat. Commun.* **5**, 4477 (2014).
54. Long, X. et al. A strongly coupled graphene and FeNi double hydroxide hybrid as an excellent electrocatalyst for the oxygen evolution reaction. *Angew. Chem. Int. Ed.* **53**, 7584–7588 (2014).
55. Wehrens-Dijkema, M. & Notten, P. H. L. Electrochemical quartz microbalance characterization of Ni(OH)₂-based thin film electrodes. *Electrochim. Acta* **51**, 3609–3621 (2006).
56. Lu, X. & Zhao, C. Electrodeposition of hierarchically structured densities. *Nat. Commun.* **6**, 1–7 (2015).
57. von Issendorff, B. & Palmer, R. E. A new high transmission infinite range mass selector for cluster and nanoparticle beams. *Rev. Sci. Instrum.* **70**, 4497–4501 (1999).
58. Pratontep, S., Carroll, S. J., Xirouchaki, C., Streun, M. & Palmer, R. E. Size-selected cluster beam source based on radio frequency magnetron plasma sputtering and gas condensation. *Rev. Sci. Instrum.* **76**, 045103 (2005).
59. Biesinger, M. C., Lau, L. W. M., Gerson, A. R. & Smart, R. S. C. The role of the Auger parameter in XPS studies of nickel metal, halides and oxides. *Phys. Chem. Chem. Phys.* **14**, 2434 (2012).
60. Biesinger, M. C. et al. Resolving surface chemical states in XPS analysis of first row transition metals, oxides and hydroxides: Cr, Mn, Fe, Co and Ni. *Appl. Surf. Sci.* **257**, 2717–2730 (2011).
61. Grosvenor, A. P., Biesinger, M. C., Smart, R. S. C. & McIntyre, N. S. New interpretations of XPS spectra of nickel metal and oxides. *Surf. Sci.* **600**, 1771–1779 (2006).

Acknowledgements

This work was supported by a research grant (9455) from VILLUM FONDEN. We also acknowledge UPCAT under project no. 2015-1-12315.

Author contributions

I.E.L.S., J.K. and I.C. conceived the experiments. C.R. participated in the conception of the experiments and performed the electrochemical measurements. B.S. participated in the conception of the experiments, prepared the nanoparticles and performed the UHV experiments. S.B.S. performed and helped in the design of the EC–MS experiments. D.B.T., P.C.K.V. and O.H. designed and helped with the interpretation of the EC–MS experiments. E.M.F. and C.D.D. performed the microscopy characterization. J.E.S. and A.B. contributed to the LEIS measurements. C.R., B.S. and S.B.S. co-wrote the manuscript. All the authors discussed the results and commented on the manuscript.

Competing interests

The authors declare no competing interests.

Additional information

Supplementary information is available for this paper at <https://doi.org/10.1038/s41929-018-0162-x>.

Reprints and permissions information is available at www.nature.com/reprints.

Correspondence and requests for materials should be addressed to I.C.

Publisher's note: Springer Nature remains neutral with regard to jurisdictional claims in published maps and institutional affiliations.

© The Author(s), under exclusive licence to Springer Nature Limited 2018